npj | computational materials

www.nature.com/npjcompumats

ARTICLE OPEN

Effect of electrode and oxide properties on the filament kinetics during electroforming in metal-oxide-based memories

Kena Zhang[1], Yao Ren[1], Panchapakesan Ganesh[2] and Ye Cao[1]✉

We developed a physical model to fundamentally understand the conductive filament (CF) formation and growth behavior in the switching layer during electroforming process in the metal-oxide-based resistive random-access memories (RRAM). The effects of the electrode and oxide layer properties on the CF morphology evolution, current-voltage characteristic, local temperature, and electrical potential distribution have been systematically explored. It is found that choosing active electrodes with lower oxygen vacancy formation energy and oxides with small Lorenz number (ratio of thermal and electrical conductivity) enables CF formation at a smaller electroforming voltage and creates a CF with more homogeneous morphology. This work advances our understanding of the kinetic behaviors of the CF formation and growth during the electroforming process and could potentially guide the oxide and electrode materials selection to realize a more stable and functional RRAM.

npj Computational Materials (2022)8:76 ; https://doi.org/10.1038/s41524-022-00770-2

INTRODUCTION

Metal oxide-based resistive random-access memory (RRAM) has been considered a promising candidate for next generation nonvolatile memory[1,2], non-volatile logic component[3], and bio-inspired neuromorphic computing[4–7], due to its fast switching speed, compatibility with the complementary metal-oxide-semiconductor (CMOS) technology[8], and easiness of fabrication[9–12]. The typical structure of an oxide-based RRAM consists of an insulating oxide layer sandwiched by a top and a bottom electrode. Its functionality stems from a conductive filament (CF), which initially forms inside the oxide layer to provide the electronic conduction pathways. The RRAM can then switch between a high resistance (HRS) and a low resistance state (LRS), as the CF evolves, ruptures and reforms between the two electrodes under the applied voltages. Depending on the type of ions that forms the CF, RRAMs can be classified into (a) electrochemical metallization devices (ECM) and (b) valence change memory devices (VCM). In the ECM device, CF is formed by metal cations that are supplied by the dissolution of the electrochemically active electrodes[13–15]. While in the VCM type, the CF is composed of defects such as oxygen vacancies ($V_o^{\cdot\cdot}$)[16–20], which are usually created inside the metal oxide-based RRAMs.

Generally, the pristine state of an as-fabricated VCM device exhibits high resistance state (HRS), and an initial one-time operation called electroforming is required to create a CF to provide a conduction channel. This is typically realized by applying a sufficiently high voltage or current on the film to form a CF of high $V_o^{\cdot\cdot}$ density inside the insulating layer to connect the top and bottom electrodes[12,21,22]. This process is determined by (i) the $V_o^{\cdot\cdot}$ generation at the oxide/electrode interface due to the chemical reactions between the oxide and the metal electrodes, and (ii) the electric field and thermal effect driven $V_o^{\cdot\cdot}$ migration in the bulk[23,24]. Therefore, the types and properties of metal electrodes could play a key role in determining the CF formation and growth behaviors. Several experimental and simulation studies have been made to understand the electrode effect on the electroforming process[22,25,26]. Chen et al.[24] studied the effect of electrode materials on the endurance/retention performance of HfO_2 based RRAMs. It was found that the long pulse endurance could be obtained by using active metals as electrodes. Nandi et al.[27] reported that the electrode roughness induced a local electrical field enhancement that reduced the forming voltage. Xu et al.[28] developed a Kinetic Monte Carlo (KMC) model to simulate the morphology of a CF in HfO_2-based RRAM, and revealed that most vacancies were generated at the metal/oxide interface due to a lower vacancy formation energy than in the bulk. However, it is still unclear how a metal electrode determines the kinetics of CF formation and growth direction, and influences the size, composition, and uniformity of the CF, which plays a critical role in determining the stability and functionality of the subsequent switching cycles[8,29,30]. Furthermore, a number of metal oxides have been used as the insulating layer in the metal oxide-based RRAMs, such as TiO_2[31], HfO_2[32], TiO_2[33], NbO[34] and etc. Unfortunately, a qualitative understanding of the effects of the physical properties of these metal oxides (such as the electrical and thermal conductivities) on the CF growth behavior during the electroforming process is still lacking. These properties could play important roles in the performances of the resistive switching behavior[35].

To address these limitations, we develop a physical model based on defect chemistry and transport theory in this work by choosing HfO_2 as a prototype to study the dynamic electroforming process in metal oxide-based RRAM. Our model well captures the formation and evolution of the conductive filament, the current-voltage characteristic, the local temperature, and electrical potential distributions during the electroforming process. Results are compared with previous experimental studies to validate the model. Based on this, we further investigate the impact of electrode properties on the growth behavior of CF. Finally, the effects of the electrical and thermal conductivity of the metal oxides on the CF growth behavior have been explored.

[1]Department of Materials Science and Engineering, University of Texas at Arlington, Arlington, TX 76019, USA. [2]Center for Nanophase Materials Sciences, Oak Ridge National Laboratory, Oak Ridge, TN 37831, USA. ✉email: ye.cao@uta.edu

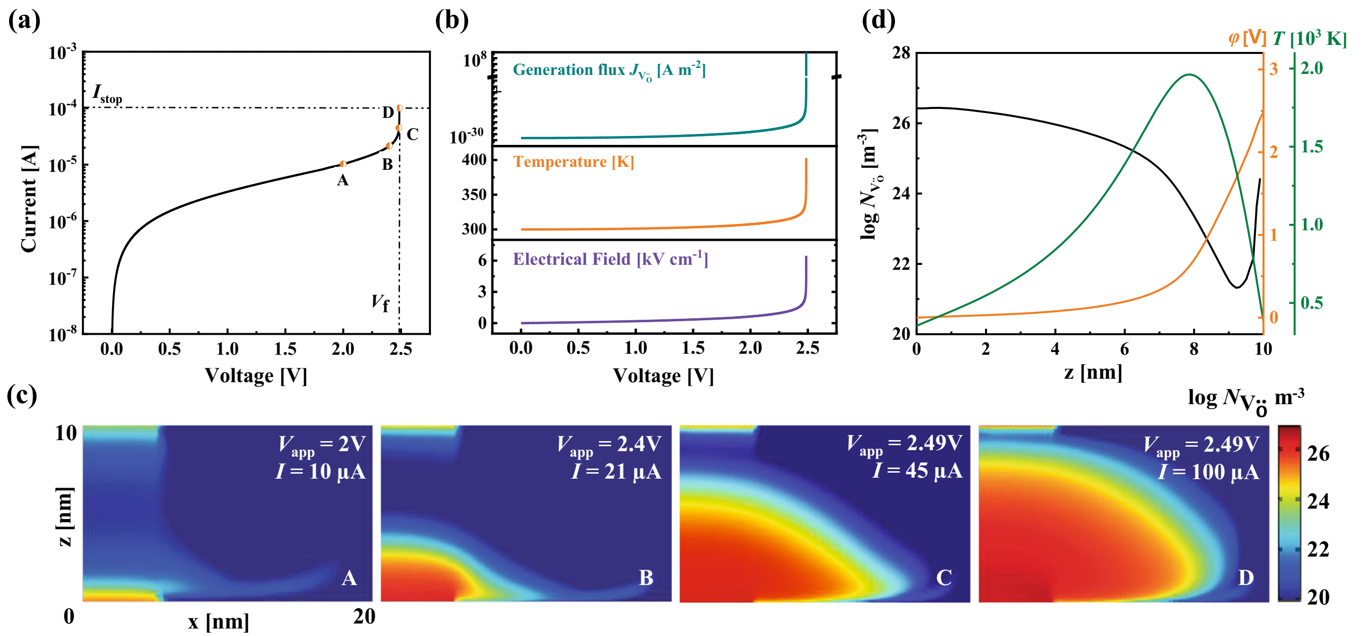

Fig. 1 Modeling electroforming process in HfO_2 metal oxide. a Current evolution characteristic by applied voltage sweep with rate dV/dt = 1 V s^{-1} and stop at I_{stop} = 100 μA. **b** The evolution of generation flux, temperature T, and electrical field E at the anodic interface (z = 10 nm). **c** Calculated 2D $N_{V_{\ddot{o}}}$ maps with increasing voltage, corresponding to state A–D in (**a**). **d** 1D profiles of $N_{V_{\ddot{o}}}$, T and φ at state D (V_f = 2.49 V) along the center of CF (x = 0, z = 0–10 nm).

RESULTS

The CF growth behavior during electroforming process

In this work, we use 2D axisymmetric model to describe the CF growth behavior during electroforming process. A 10 nm HfO_2 is sandwiched between 50 nm Pt bottom electrode and 20 nm Ta top electrode where a voltage sweep rate (dV/dt) of 1 V s^{-1} is applied on the top electrode and the bottom electrode is grounded. Initially, the oxide layer is at high resistance state with relatively low oxygen vacancy density, which is assumed to be uniformly distributed in the oxide layer, at a concentration of $N_{V_{\ddot{o}}} = 6 \times 10^{19}$ m^{-3}. We assume the oxygen exchange is taken place at the interface between HfO_2 and Ta anode with a vacancy formation barrier of 2.5 eV[24] which determines the rate of interface $V_o^{\cdot\cdot}$ gerneration in a confined region. The physical dynamics of $V_o^{\cdot\cdot}$ generation and migration are controlled by Eqs. (4–8) (see "Methods" for details). The simulation stops when the current (I_{stop}) reaches 100 μA where, in experimental case, this current is always used to avoid permanent breakdown[36].

Figure 1a shows the current evolution characteristic. It is clearly seen that the current increases exponentially during the electroforming process. Initially, the current of the device increases gradually until the forming voltage (V_f = 2.49 V), where an abrupt increase of current is seen. This indicates that the electroforming process occurs at a critical threshold voltage, instead of a cumulative phenomenon in the filament growth. The current increase is due to the increasing $V_o^{\cdot\cdot}$ concentration, which is influenced by the $V_o^{\cdot\cdot}$ generation rate at the anodic interface. To further understand this behavior, we plotted the evolutions of the $V_o^{\cdot\cdot}$ generation rate, the electrical field, and the temperature at the anodic interface under applied voltage sweep, as shown in Fig. 1b. It is seen that the initial generation rate is small and gradually increases with the increasing voltage due to the lower electrical field and temperature. When the forming voltage reaches V_f, the sudden increases of the electrical field and temperature at the anodic interface give rise to a self-acceleration of the $V_o^{\cdot\cdot}$ generation flux at a very short time as shown in Fig. 1b. This results in an abrupt electroforming transition. Figure 1c illustrates the 2D maps of the oxygen vacancy distribution ($N_{V_{\ddot{o}}}$) at different stages, corresponding to the points A to D as marked in Fig. 1a. It is seen that $V_o^{\cdot\cdot}$ are generated at the anode interface and start to accumulate to the cathode when the voltage is up to 2 V, as shown in Fig. 1c (A). At this stage, the concentration of $V_o^{\cdot\cdot}$ is small due to the small generation rate. Along with the applied voltage, more $V_o^{\cdot\cdot}$ are generated at anode and gradually accumulate near the cathode resulting a local segregation, as shown in Fig. 1c (B). As the applied voltage further increases to V_f, massive $V_o^{\cdot\cdot}$ are generated and migrate towards the cathode immediately, and the CF length increases suddenly resulting in a small $V_o^{\cdot\cdot}$ depletion gap near the anode, as shown in Fig. 1c (C) and (D). Figure 1d illustrates the 1D profiles of the oxygen vacancy density $N_{V_{\ddot{o}}}$, temperature T, and electrical potential φ along the cylindrical symmetry axis (x = 0, z = 0–10 nm) at the final electroforming state D. Here we only plot T and φ inside the oxide layer (z = 0–10 nm) as their variations inside the top and bottom electrodes are negligible. Compared to the initial oxygen vacancy density ($N_{V_{\ddot{o}}} = 6 \times 10^{19}$ m^{-3}), the final $N_{V_{\ddot{o}}}$ near the cathode increases by almost 10^7, indicating the occurrence of Mott transition. Due to the tunneling or thermal emission effect, the electron transport overcomes a low energy barrier, the semiconductor has undergone a Mott transition[37]. Therefore, the critical vacancy concentration (N_c) at Mott transition for HfO_2 is assumed to be ~10^{25} m^{-3}, which is lower than oxygen vacancy concentration of 0.2×10^{27} m^{-3} where E_{AC} = 0 eV. As the $V_o^{\cdot\cdot}$ accumulation near the cathode and a depletion gap near the anode, the electrical potential dramatically drops near the anode, and remains almost constant in the highly conductive CF region near the cathode, which results in a local enhancement of electrical field and temperature near the anode region. The local enhancements of temperature and electrical field further increase the $V_o^{\cdot\cdot}$ mobility and promote the $V_o^{\cdot\cdot}$ migration from the gap region to the cathode. In this case, the $V_o^{\cdot\cdot}$ generation rate is slightly limited and cannot fully compensate the $V_o^{\cdot\cdot}$ migration rate from anode to cathode. Therefore, a small $V_o^{\cdot\cdot}$ depletion region ($N_{V_{\ddot{o}}} < N_c$) inside the CF is observed near the anode (z = 10 nm), while the $N_{V_{\ddot{o}}}$ in the remaining part of CF is higher than N_c. Based on these studies, it can be inferred that the generation rate of $V_o^{\cdot\cdot}$ at the interface

Published in partnership with the Shanghai Institute of Ceramics of the Chinese Academy of Sciences

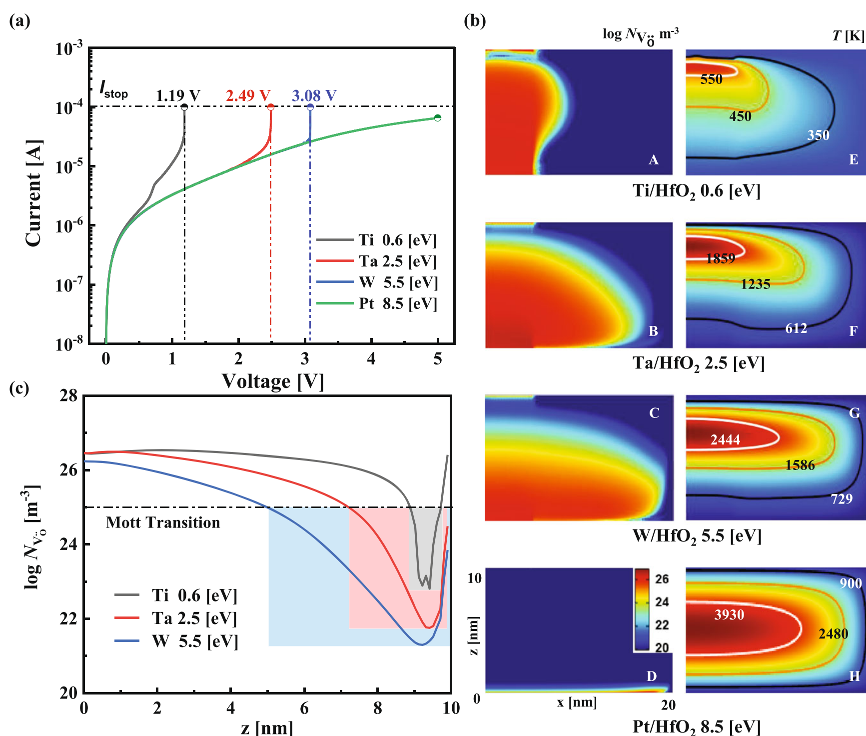

Fig. 2 Effect of electrode properties on the CF growth. a Current evolution characteristics with different electrode materials under an applied voltage sweep with rate $dV/dt = 1\ V\ s^{-1}$ and stop at $I_{stop} = 100\ \mu A$ or $V_{app} = 5\ V$. **b** 2D maps of distributions of $N_{V_{\ddot{o}}}$ and temperature T at final state. **c** 1D profiles of $N_{V_{\ddot{o}}}$ along the center of CF ($x = 0$, $z = 0$–10 nm) at the final state (the blue, red, and gray shades indicate the position and width of the oxygen vacancy depletion gap).

and the migration of $V_{\ddot{o}}$ in the bulk influence the CF morphology and growth behavior.

The CF growth behavior and I–V characteristic simulated from the current model agree well with previous experimental reports on HfO_2-based[24,27,38] device. For example, Chen et al.[25] found that the forming voltage for HfO_2 based RRAM with Ta anode is about 3 V, which is slightly higher than our simulation result ($V_f = 2.49$ V). This is probably because the area of the switching cell in their experiment is larger than our simulation. Other experimental results of metal oxide-based RRAMs[36,37,39–41] also show that the soft breakdown of the insulating layer occurs when the voltage sweep is applied, followed by a dramatic current increase at a critical threshold voltage (V_f) during the electroforming process, which agrees with our simulation results. Therefore, in the following sections we will employ this model to investigate the effects of the electrode materials and the metal oxide properties on the CF growth behavior during the electroforming process and derive a general principle for materials selection of both metal electrodes and oxide layer in RRAMs.

Effect of electrode properties on the CF growth behavior

The oxygen vacancy generation rate at the anodic interface is strongly dependent on the anode properties, i.e., the ability to extract oxygen atoms from HfO_2. Active metal electrodes (such as Hf, Ti, Ta, etc.) show lower vacancy formation barrier than inert electrodes (such as W, Ru, Pt, etc.). To fully understand the effect of different electrodes on the CF growth behavior, we choose Ti, Ta, W and Pt as the anode electrode with an increasing vacancy formation barrier E_b of 0.6, 2.5, 5.5, and 8.5 eV, respectively[24]. A voltage sweep with rate of $dV/dt = 1\ V\ s^{-1}$ is applied on the anode, and the simulation is stopped at $I_{stop} = 100\ \mu A$ or $V_{app} = 5$ V, whichever comes first. Figure 2a illustrates the temporal evolutions of the overall current with different anode materials (Ti, Ta, W, and Pt). The currents in all cases increase exponentially with increasing voltage, followed by an abrupt increase at different forming voltages except for Pt. Based on our calculations, it is found that electrodes with higher vacancy formation energy require larger forming voltages for the CF formation, as shown in Fig. 2a and Supplementary Fig. 1. The Ti electrode with the smallest E_b is found to be able to form CF at the smallest forming voltage $V_f = 1.19$ V. In contrast, the device with inert Pt electrode doesn't show the abrupt increase in current even after the applied voltage reaches 5 V.

Figure 2b shows the 2D maps of the final $V_{\ddot{o}}$ density and the temperature distributions with different metal anodes. Figure 2c compares the corresponding 1D profiles of $N_{V_{\ddot{o}}}$ along the center of CF ($x = 0$, $z = 0$–10 nm) and the width of the depletion gaps. These results indicate that the interfacial properties significantly affect the final morphology of the CF. When E_b is small (Ti/HfO_2 interface), the $V_{\ddot{o}}$ distribution is more homogeneous in the CF region, with a very small $V_{\ddot{o}}$ depletion gap near the anode. As E_b increases, the width of the depletion gap increases, and $N_{V_{\ddot{o}}}$ in the CF becomes highly inhomogeneous as the shadows shown in Fig. 2c. It is also observed from Fig. 2b (A–C) that $V_{\ddot{o}}$ migrate along the radial (x) direction and broaden the CF width with increasing E_b. The inhomogeneous morphology of CF is due to the enhanced forming voltage (V_f) which further promotes the $V_{\ddot{o}}$ migration from the anode to the cathode region, resulting in a wider depletion gap. On the other hand, the increasing electrical field causes temperature increase at the gap region (Fig. 2b (E, F)) based on the Joule heating effect, which further facilitates the $V_{\ddot{o}}$ diffusion and eventually causes the lateral broadening of the CF. Moreover, the CF is not able to form with the inert Pt electrode ($E_b = 8.5$ eV) even when the applied voltage reaches 5 V, and the corresponding temperature becomes extremely high. To create CFs in HfO_2 with Pt electrode, a much higher voltage is needed, under which the $V_{\ddot{o}}$ tend to generate from the interior of the oxide rather than the interface controlled CF growth[27].

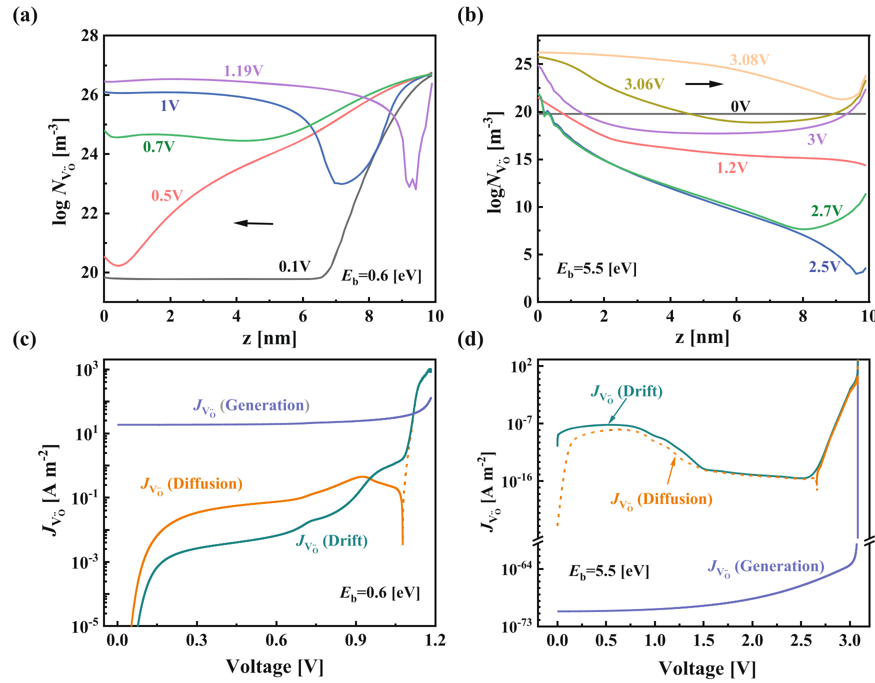

Fig. 3 The competition between generation rate and migration rate. a, b The evolution of distributions of $N_{V_o^{..}}$ along the center of CF ($x = 0$, $z = 0$–10 nm) with an active electrode Ti and an inner electrode W under a voltage sweep rate dV/d$t = 1$ V s^{-1}. **c, d.** The generation flux at the point in interface ($x = 0$, $z = 10$ nm), the drift and diffusion flux at the point near the anode ($x = 0$, $z = 8.5$ nm) with Ti and W electrodes, respectively. Flux direction from anode to cathode is marked as solid line, while flux direction from cathode to anode is marked as dotted line.

To further understand the dynamic during electroforming process, in particularly the CF growth direction, we investigate the interplay between the $V_o^{..}$ generation at the anodic interface and the $V_o^{..}$ migration in the bulk of HfO_2 with different metal electrodes. Figure 3a and b illustrate the 1D temporal evolutions of $N_{V_o^{..}}$ along the center axis ($x = 0$, $z = 0$–10 nm) with active anode Ti ($E_b = 0.6$ eV) and inert anode W ($E_b = 5.5$ eV), respectively. The flux due to the $V_o^{..}$ generation at the anodic interface ($x = 0$, $z =$ 10 nm), and the flux due to $V_o^{..}$ drift and diffusion near the anodic interface ($x = 0$, $z = 8.5$ nm) under the applied voltage sweep are compared in Fig. 3c, d, respectively. From Fig. 3a, it is seen that $N_{V_o^{..}}$ near the anode quickly increases above N_c and reaches ~10^{27} m^{-3}. This is because the generation flux reaches above 10 A m^{-2} (blue curve in Fig. 3c), which is much higher than the initial migration flux (diffusion and drift). When the applied voltage increases from 0.1 to 0.7 V, $V_o^{..}$ created near the anode ($z = 10$ nm) gradually migrates to cathode. The filament consisting of relatively high $N_{V_o^{..}}$ starts to grow from the anode toward the cathode (indicated by the arrow in Fig. 3a). In this period, the $V_o^{..}$ migration to cathode is driven by the diffusion and drift flux, while the contribution of diffusion is larger than drift due to a large concentration gradient caused by the higher generation rate at the anodic interface. When the voltage increases to ~1 V, $V_o^{..}$ can easily be removed from the anode and migrate to the cathode which results in an increasing drift flux (green curve in Fig. 3c). Consequently, the $N_{V_o^{..}}$ near the cathode eventually increases above N_c, and a $V_o^{..}$ depletion gap is created near the anode region (blue curve in Fig. 3a). When V_{app} further increases to 1.19 V, the $N_{V_o^{..}}$ near cathode continues to increase and reaches ~10^{27} m^{-3}, the width of the depletion gap decreases, and the location of this gap moves towards the anode. The formation of the depletion gap induces a negative $V_o^{..}$ concentration gradient (from cathode to anode) and a negative diffusion flux (as indicated by the orange dotted curve in Fig. 3c), which partially offsets the positive drift flux (solid green curve in Fig. 3c) and drives the $V_o^{..}$ diffusion towards the anode to reduce the width of the depletion gap. Our analyses demonstrate that for active anode, the CF growth direction is from anode to cathode and a relatively uniform CF is eventually formed, as the arrow shown in Fig. 3a.

Figure 3b, d represents the CF growth dynamic under a relatively inert electrode (W) with higher $E_b = 5.5$ eV. The initial $V_o^{..}$ is uniform in the oxide layer at $V_{app} = 0$ V. When the applied voltage increases, the $V_o^{..}$ are depleted near the anode and pile up near the cathode, which creates a wide depletion gap near the anode, as shown in Fig. 3b. This is because the positive drift flux (solid green curve in Fig. 3d) is much larger than the flux due to $V_o^{..}$ generation at the anodic interface (solid blue curve in Fig. 3d), and the negative diffusion flux (dotted orange curve in Fig. 3d) only partially offsets the drift flux. When the applied voltage further increases, the $V_o^{..}$ generation flux and $N_{V_o^{..}}$ start to increase near the anode and further migrate towards the cathode as the increasing drift and diffusion flux both contribute to the migration flux from anode to cathode. Consequently, a CF with a higher concentration $N_{V_o^{..}} > N_c$ first appears at the cathode side (3.0 V state in Fig. 3b) and continues to grow towards the anode when voltage is above 3.0 V, as indicated by the arrow in Fig. 3b.

Effects of oxide properties on the CF growth behavior

Our simulation results indicate that the local electrical field and temperature strongly affect the oxygen vacancy transport and thus the CF growth. From Eqs. 5 and 7, the electrical and thermal transports are highly dependent on the oxide properties, such as the electrical (σ) and thermal conductivity (k_{th}) of the host metal oxides. Since σ and k_{th} in the metal oxides are much smaller than their corresponding metallic states, for simplicity, we assume that σ and k_{th} are the same for different pristine oxides (such as TiO_2, HfO_2, etc.), and are linearly extrapolated to their values in the corresponding metallic states as a function of increasing $N_{V_o^{..}}$. Based on this assumption, we can easily represent the σ and k_{th} for different metal oxides by tunning the slopes of the linear curve, i.e., K_1 and K_2 (see "Methods" for more details).

Figure 4 illustrates the effect of electrical conductivity on the CF growth. Here, in order to study the effect of electrical conductivity

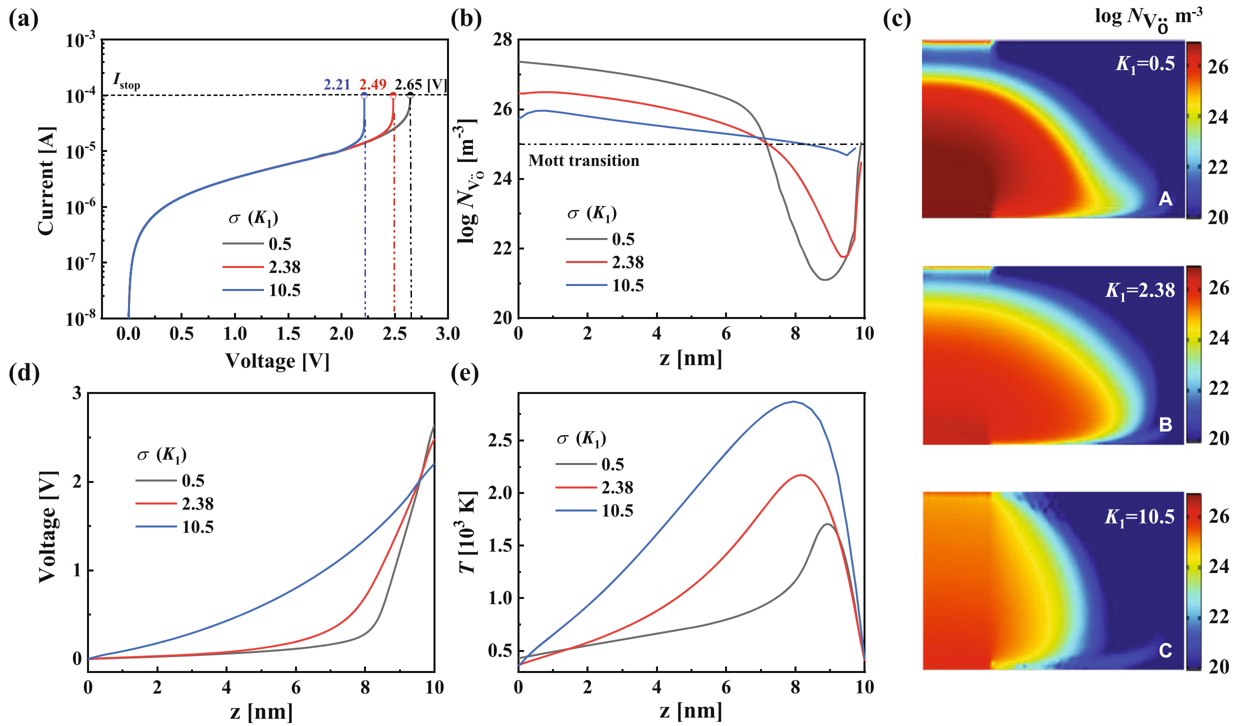

Fig. 4 Effect of electrical conductivity on the CF growth. **a** Current characteristic with different electrical conductivity (by K_1) under a voltage sweep rate $dV/dt = 1\,V\,s^{-1}$. **b** $N_{V_{O}^{\cdot\cdot}}$ distributions along the center of CF ($x = 0$, $z = 0$–10 nm) at final state. **c** Calculated 2D $N_{V_{O}^{\cdot\cdot}}$ map. **d**, **e** Calculated 1D profiles of local electrical potential φ and temperature T along the center of CF ($x = 0$, $z = 0$–10 nm) at final state.

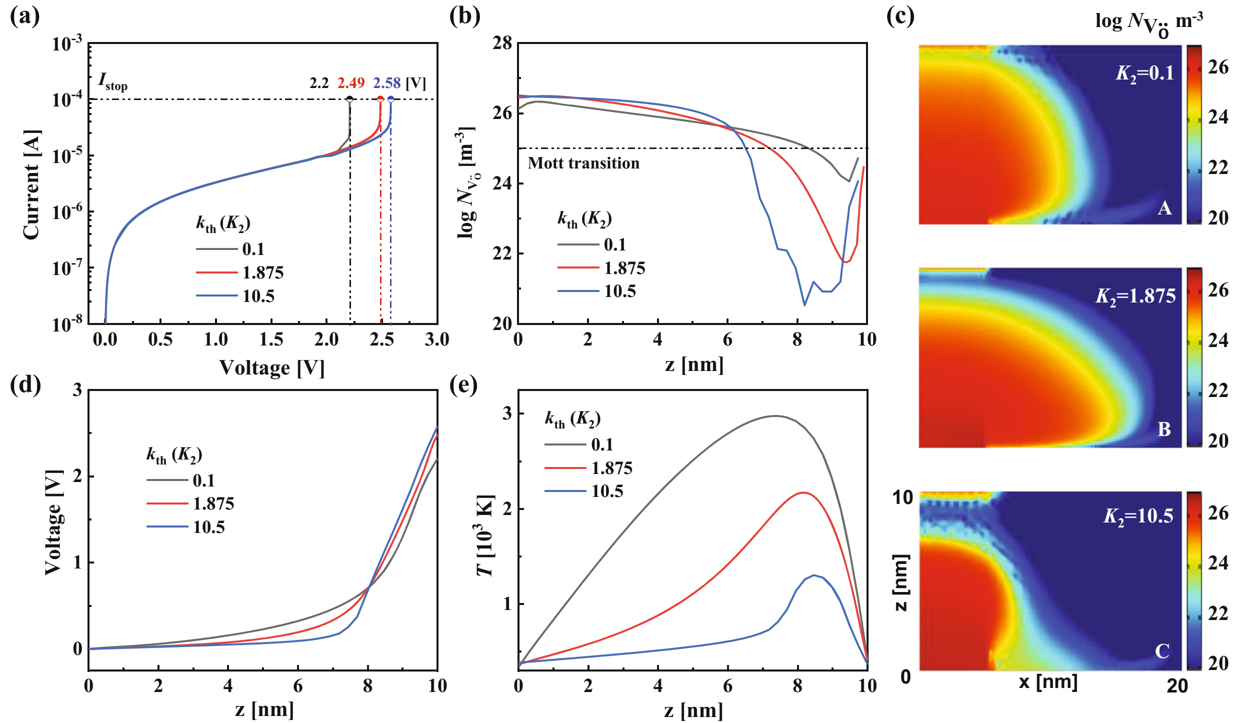

Fig. 5 Effect of thermal conductivity on the CF growth. **a** Current characteristic with different thermal conductivity (by K_2) under a voltage sweep rate $dV/dt = 1\,V\,s^{-1}$. **b** $N_{V_{O}^{\cdot\cdot}}$ ditributions along the center of CF ($x = 0$, $z = 0$–10 nm) at final state. **c** Calculated 2D $N_{V_{O}^{\cdot\cdot}}$ map. **d**, **e** Calculated 1D profiles of local electrical potential φ and temperature T along the center of CF ($x = 0$, $z = 0$–10 nm) at final state.

on the CF growth, we assume the vacancy formation barrier is a constant ($E_b = 2.5$ eV). The total current evolution with different electrical conductivities (represented as $K_1 = 0.5$, 2.38, and 10.5) is shown in Fig. 4a. While the initial current evolutions are almost the same for different K_1, the forming voltage (V_f), as indicated by a sudden increase of total current, decreases monotonously with the increasing electrical conductivity (K_1). Figure 4c illustrates the 2D maps of the final $V_o^{\cdot\cdot}$ distribution with different electrical conductivities, and the corresponding 1D $N_{V_o^{\cdot\cdot}}$ profiles along vertical ($x = 0$, $z = 0$–10 nm) are shown in Fig. 4b. A larger $V_o^{\cdot\cdot}$ depletion gap is observed under lower electrical conductivity ($K_1 = 0.5$), which diminishes in size with increasing electrical conductivity of the oxide. As K_1 reaches 10.5, the $N_{V_o^{\cdot\cdot}}$ becomes homogenous and the CF becomes uniform in morphology. The 1D electrical potential and the local temperature distributions along vertical direction ($x = 0$, $z = 0$–10 nm) at the final forming states with different electrical conductivities are compared in Fig. 4d, e. As shown in Fig. 4e, the heat generation by Joule heating effect is reduced when σ is low ($K_1 = 0.5$) (black curve in Fig. 4e). Consequently, the $V_o^{\cdot\cdot}$ generation rate becomes low under lower temperature, and a larger V_f is needed to create a CF (Fig. 4a). The higher applied voltage accelerates the $V_o^{\cdot\cdot}$ migration from anode to cathode, resulting in a local segregation of $V_o^{\cdot\cdot}$ at the cathode. The region of higher oxygen vacancy density exhibits lower resistance. As a result, the electrical voltage remains constant from the cathode towards the inside bulk. The resistance of the $V_o^{\cdot\cdot}$ depletion gap is higher than that of the $V_o^{\cdot\cdot}$ segregation region, so that a large voltage drop along the gap region is observed (black curve in Fig. 4d). This results in a local enhancement of electrical field (Supplementary Fig. 2), which further accelerates the $V_o^{\cdot\cdot}$ migration and accumulation near the cathode, and eventually induces a large depletion gap near $z = 8$ nm (Fig. 4b, c). When σ increases ($K_1 = 2.38$), more heat is generated (red curve in Fig. 4e) to prompt the $V_o^{\cdot\cdot}$ generation and reduce the forming voltage of the CF. Compared with the case $K_1 = 0.5$, the smaller local electric field enhancement (red curve in Fig. 4d and Supplementary Fig. 2) reduces the driving force for $V_o^{\cdot\cdot}$ migration towards cathode, resulting in a smaller depletion gap. When $K_1 =$ 10.5, a large amount of heat is produced, and a higher local temperature is seen near the anode due to a larger electrical conductivity (blue curve in Fig. 4e). This leads to a larger $V_o^{\cdot\cdot}$ generation flux and a reduction of forming voltage that reduce the local enhancement of the electrical field (blue curve in Fig. 4d and Supplementary Fig. 2) and slows down the $V_o^{\cdot\cdot}$ drift to cathode. On the other hand, the temperature increase promotes the $V_o^{\cdot\cdot}$ diffusion from the cathode region of high $V_o^{\cdot\cdot}$ concentration towards the $V_o^{\cdot\cdot}$ depletion gap to reduce the concentration gradient, and eventually offsets the $V_o^{\cdot\cdot}$ drift by the local electric field. Consequently, the $V_o^{\cdot\cdot}$ depletion gap near the anode and the $V_o^{\cdot\cdot}$ segregation near the cathode almost disappear (blue curve in Fig. 4b), and the uniformity of the $V_o^{\cdot\cdot}$ concentration inside the CF is significantly improved (snapshot C in Fig. 4c).

Figure 5 illustrates the effect of thermal conductivity k_{th} (by the slope K_2) on the CF growth. Here, we apply the same boundary conditions of electrical bias as the electrical conductivity case. Figure 5a shows the temporal evolution of total current with different k_{th} (represented as $K_2 = 0.1$, 1.875, and 10.5). The lower k_{th} ($K_2 = 0.1$) results in a higher temperature (black curve in Fig. 5e) which promotes the $V_o^{\cdot\cdot}$ generation at a reduced forming voltage of 2.2 V (Fig. 5a). In this case, the induced $V_o^{\cdot\cdot}$ migrates to the cathode and shows a slight segregation in cathode region, because the drift flux from anode to cathode is suppressed due to the decreasing local electrical field (black curve in Fig. 5d and Supplementary Fig. 2). On the other hand, the diffusion flux from cathode to anode is highly enhanced due to the high temperature and partially cancels the drift flux. Consequently, a CF with more uniform $N_{V_o^{\cdot\cdot}}$ distribution and a much smaller $V_o^{\cdot\cdot}$ depletion gap is formed (snapshot A in Fig. 5c and black curve in Fig. 5b). As the k_{th} (K_2) increases, the heat generated by Joule heating effect can be easily dissipated and the local temperature decreases (red curve in Fig. 5e), which inhibits the $V_o^{\cdot\cdot}$ generation and increases the CF forming voltage up to 2.49 V (Fig. 5a). When k_{th} further increases ($K_2 = 10.5$), the induced $V_o^{\cdot\cdot}$ migration from anode to cathode becomes much easier under a higher local electrical field (blue curve in Fig. 5d and Supplementary Fig. 2). Thus, more $V_o^{\cdot\cdot}$ accumulation near the cathode and a larger $V_o^{\cdot\cdot}$ depletion gap near the anode is clearly seen (snapshot C in Fig. 5c and blue curve in Fig. 5b).

DISCUSSION

Based on our simulations, it is revealed that the CF growth behavior is determined by both the electrode properties (energy barrier of metals to oxidize from oxide E_b) and the physical properties of the oxides (the electrical and thermal conductivity). It is found that employing active metal electrode accelerates the formation of a CF and improves the homogeneity of the CF concentration. That's why active metals such as Ti and Ta with small vacancy formation barrier (E_b) and large capability to extract oxygen atoms from oxides are widely used as the electrode materials[42–44]. Lee et al.[42] reported a novel HfO_2 based resistive memory with TiN/Ti/HfO_2/TiN stacking layers. Due to the high activity of a Ti layer inserted between the HfO_2 and electrode TiN, large amount of oxygen can be exchanged between Ti and HfO_2, resulting in the formation of HfO_x ($x \sim 1.4$) of high oxygen deficiency. Yang et al.[45] demonstrated that Ta metal electrode could serve as a large reservoir of mobile oxygen vacancies in Pb/TaO_x/Ta system. In the case when the electrode is blocking for oxygen exchange at the metal/oxide interface, additional oxygen exchange layers (OEL) attached on the electrodes can also potentially improve the $V_o^{\cdot\cdot}$ generation rate[39,46]. Our simulation work manifests that controlling the electrode properties can be used to design and optimize the properties of metal oxide-based RRAMs.

On the other hand, our analyses show that the interplay between the $V_o^{\cdot\cdot}$ generation rate at the anodic interface and the $V_o^{\cdot\cdot}$ migration rate in the bulk strongly influences the CF growth direction during the electroforming process. When the $V_o^{\cdot\cdot}$ generation rate is much smaller than the $V_o^{\cdot\cdot}$ migration rate in the bulk, a local conductive region is first formed near the cathode where $V_o^{\cdot\cdot}$ are segregated due to the fast migration. Then the CF continues to grow towards the anode region, when $V_o^{\cdot\cdot}$ diffuse back from cathode to anode. When the $V_o^{\cdot\cdot}$ generation rate is larger than and the $V_o^{\cdot\cdot}$ migration rate in the bulk, the generated $V_o^{\cdot\cdot}$ at the anode site diffuse and drift gradually towards the cathode, such that the CF propagates from the anode towards the cathode. Specifically, the filament growth in different directions has been observed and our simulation results are consistent with experimental results[15].

Finally, it is revealed that the increase of electrical conductivity in oxide can generate more heat by Joule heating effect, and can thus enhance the $V_o^{\cdot\cdot}$ generation rate and decrease the forming voltage of the CF. Meanwhile, the increase of thermal conductivity promotes the heat dissipation and reduces the $V_o^{\cdot\cdot}$ generation rate, resulting in a higher forming voltage. Higher forming voltage further promotes $V_o^{\cdot\cdot}$ generation at the anodic interface and accelerates the $V_o^{\cdot\cdot}$ drift to the cathode, creating a large $V_o^{\cdot\cdot}$ depletion gap. Based on these studies, we can conclude that choosing metal oxides with high electrical conductivity and lower thermal conductivity helps to improve the uniformity of the CF with homogeneous $V_o^{\cdot\cdot}$ concentration and reduce the electroforming voltage. Based on the Wiedemann–Franz law, for nearly-free electron metals, the ratio of the electronic contribution of the thermal conductivity (k_{th}) to the electrical conductivity (σ) is proportional to the temperature (T), i.e., $\frac{k_{th}}{\sigma} \sim LT$, where L is the Lorenz number. Theoretically, L should be the same for different

Published in partnership with the Shanghai Institute of Ceramics of the Chinese Academy of Sciences

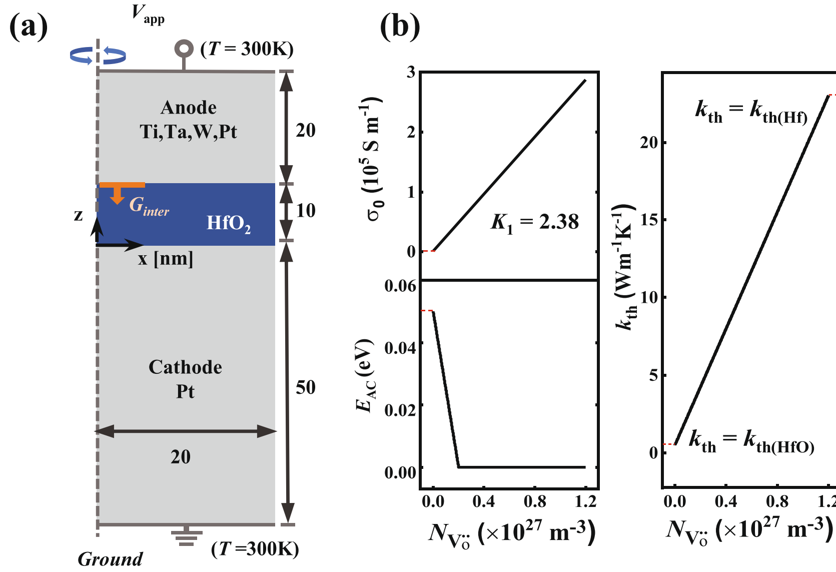

Fig. 6 Model geometry and Simulation parameters. a Model size and geometry. Voltage is applied at the top electrode (anode) and the bottom electrode (cathode) is grounded. Oxygen exchange is assumed to take place at the interface between anode and oxide in a confined region ($x = 0$–5, $z = 10$ nm). **b** Electrical conductivity preexponential factor σ_0, activation energy for conduction E_{AC}, thermal conductivity k_{th} as a function of local oxygen vacancy density $N_{V_o^{..}}$[38,56].

pure metals at identical temperatures. However, for binary transition metal oxides that have strong electron–electron correlations, L could be lowered by several orders of magnitude due to a very low electronic thermal conductivity[47,48]. Therefore, our study provides a guidance for future materials selection of metal oxide-based RRAM, i.e., to choose metal oxides with a relatively lower Lorenz number at the same temperature to achieve uniform CF during the electroforming process.

In summary, a physical model is developed to quantitatively understand the main physical mechanisms and kinetic factors that control the electroforming process. It is found that the conductive filament (CF) growth and final morphology are influenced by the electrode properties. By choosing active electrodes with low vacancy formation barrier E_b, a highly uniform CF can be formed at a much lower forming voltage. It is further revealed that the competition between the oxygen generation rate at the anode and the oxygen vacancy migration rate through the oxide layer controls the CF growth direction. When $V_o^{..}$ generation rate is higher than the migration rate, such as with anode that has a low impedance for oxygen exchange, the conductive filament is initially formed in the anode region and continues to grow towards the cathode. Otherwise, the CF is first formed in the cathode region and grows in the opposite direction. Finally, the effects of materials properties of the oxide, i.e., the electric and thermal conductivity in different metal oxides-based RRAM are investigated. For metal oxides-based RRAM with higher electric conductivity and lower thermal conductivity, homogenous CF morphology is generated. Our work provides a comprehensive understanding of the effects of both electrode properties and internal materials properties on the CF formation and could further guide the materials selection and the electrode treatment to achieve a homogenous and uniform CF at reduced forming voltages.

METHODS

During the electroforming process, a CF is formed and eventually connects one electrode to the other. In most metal oxides-based RRAM devices, this process is controlled by the generation of $V_o^{..}$ at the anode/oxide interface[15,27,33,43,49] and the migration of $V_o^{..}$ in the oxide layer, which is driven by the electrical field and Joule heating effect. Therefore, in our model, the oxygen vacancy density ($N_{V_o^{..}}$) is selected as the field variable and the total free energy of the system (f_{total}) will be calculated as a function of $N_{V_o^{..}}$. Here we only consider the chemical and electrical energy contributions to the total free energy, and use an ideal solution model to describe the chemical energy of the system, i.e.,

$$\begin{aligned} f_{total} &= f_{chem} + f_{electric} \\ &= -k_BT\left[N_o \ln\frac{N_o}{N_o - N_{V_o^{..}}} + N_{V_o^{..}} \ln\frac{N_o - N_{V_o^{..}}}{N_{V_o^{..}}}\right] + \left[2eN_{V_o^{..}}\varphi - \tfrac{1}{2}\varepsilon_0\varepsilon_r(\nabla\varphi)^2\right] \end{aligned} \quad (1)$$

where k_B is the Boltzmann constant, T is the temperature, $N_o, N_{V_o^{..}}$ are the total number of lattice sites of oxygen atoms and the number of oxygen vacancies, e is the elementary charge, φ is the electrical potential, ε_0 and ε_r are the vacuum permittivity and relative permittivity, respectively. The chemical potential of the system ($\mu_{V_o^{..}}$) can be calculated by taking the variational derivative of f_{total} over $N_{V_o^{..}}$, i.e.,

$$\mu_{V_o^{..}} = \frac{\delta f_{total}}{\delta N_{V_o^{..}}} = k_BT \ln\frac{N_{V_o^{..}}}{N_o - N_{V_o^{..}}} + 2e\varphi \quad (2)$$

And the flux of the oxygen vacancy migration ($J_{V_o^{..}}$) is defined to be linearly proportional to the chemical potential gradient ($\nabla\mu_{V_o^{..}}$):

$$J_{V_o^{..}} = -\frac{D}{k_BT} N_{V_o^{..}} \nabla\mu_{V_o^{..}} \quad (3)$$

where D is the diffusivity of $V_o^{..}$, which is assumed to be temperature-dependent through the Arrhenius relation $D = D_0 e^{-\frac{E_a}{k_BT}}$. Here D_0 is the pre-exponential factor of diffusivity and E_a is the diffusion energy barrier. In this work, we use $D_0 = 2 \times 10^{-3}\,\mathrm{cm}^2\,\mathrm{s}^{-1}$ and $E_a = 1$ eV based on literature[50]. The migration of positively charged $V_o^{..}$ can thus be described by the Nernst–Planck equation,

$$\frac{\partial N_{V_o^{..}}}{\partial t} = -\nabla \cdot J_{V_o^{..}} = \nabla \cdot \left(D\nabla N_{V_o^{..}} + \frac{eD}{k_BT} N_{V_o^{..}} \nabla\varphi\right) \quad (4)$$

We simulate the resistance change based on an ohmic current model for electronic conduction, with a local inhomogeneous electrical conductivity determined by the oxygen vacancy concentration. Since electrons are of much higher mobility than oxygen vacancies, they are thus assumed to be always able to compensate the excessive charges induced by the oxygen vacancies along the CF. Due to the fact that the external oxygen vacancy transport time scale is much longer than the electron relaxation time (see detailed calculations in Supplementary Note), the quasi-steady current continuity equation ($\nabla \cdot J = 0$) is used to calculate the electrical potential. The current density ($J = \sigma E$) calculated by Ohm's law depends on the local electrical conductivity (σ) and the local electrical field ($E = -\nabla\varphi$). Thus, the

current continuity equation can be rewritten as,

$$\nabla \cdot \sigma \nabla \varphi = 0 \tag{5}$$

And the total current is calculated by a cross-section integral

$$I = \int \sigma \nabla \varphi \, ds \tag{6}$$

Finally, the Fourier heat-flow equation is solved to calculate the local temperature profile. The transient contribution ($\rho C_p \cdot \frac{\partial T}{\partial t}$) to the Fourier equation can be safely ignored[50] due to a faster thermal response of approximately ~10 ps, which means that the time when the electrons and lattice reach thermal equilibrium are much shorter than the time scale of oxygen vacancy transport (see detailed calculations in Supplementary Note).

$$-\nabla \cdot k_{\mathrm{th}} \nabla T = \sigma |\nabla \varphi|^2 \tag{7}$$

where σ and k_{th} are the electrical and thermal conductivity, respectively.

Generally, the $V_o^{\cdot\cdot}$ can be created either from a Frenkel pair inside the bulk oxide, or at the active anode/oxide interface where the oxygen atoms are extracted from the oxide through the following chemical reaction[24]:

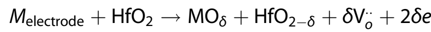

$$M_{\mathrm{electrode}} + \mathrm{HfO_2} \rightarrow \mathrm{MO}_\delta + \mathrm{HfO}_{2-\delta} + \delta V_o^{\cdot\cdot} + 2\delta e$$

In most metal-oxide-metal systems, the vacancy formation energy at active-anode/HfO_2 interface[24,28,49] is much lower than the formation energy of a Frenkel pair in the bulk oxide[27,28,51,52]. Therefore, the electroforming process is mainly controlled by the generation of $V_o^{\cdot\cdot}$ at the active-anode/oxide interface, which have been reported in many metal oxide-based RRAMs[15,43,44,53]. In light of this, we ignore the bulk generation of $V_o^{\cdot\cdot}$ and assume that the $V_o^{\cdot\cdot}$ generation only occurs at the active anode/oxide interface. This enables us to focus on investigating the electrode properties on the CF growth behavior. The $V_o^{\cdot\cdot}$ generation rate at the anodic interface G_{inter} is determined by

$$G_{\mathrm{inter}} = G_1 \cdot \left[\exp\left(\frac{-(E_b - e\beta E)}{k_B T} \right) \right] \tag{8}$$

where G_1 is pre-exponential factor for interface generation rate, E_b is the vacancy formation barrier, e is the elementary charge, β is the field enhancement factor, E is the local electrical field, k_B is the Boltzmann's constant, and T is the local temperature. The term $e\beta E$ describes the energy barrier lowering due to the applied field. According to Eq. 8, the interface vacancy formation energy (E_b) determines the rate of oxygen atom extraction from the oxide (i.e., the interface $V_o^{\cdot\cdot}$ generation rate), which is a characteristic variable for different electrode materials[24]. Therefore, we select both chemically active metals (Ti and Ta) and inert metals (W and Pt) as anodes with different values of E_b to understand the effect of anode materials on the CF growth behavior during the electroforming process. It is found that the CF is preferentially created from high-aspect-ratio asperities due to the local electrical field enhancement[27], or from a seed like the pre-existing fabricated defects at the interface with lower vacancy formation barrier[54] rather than the entire electrode. For simplicity, we assume that the oxygen exchange only takes place at the interface between the anode and oxide in a confined region ($x = 0$–5, $z = 10$ nm) without consideration of the effect of the electrode roughness or the pre-existing interface defects. This allows us to focus only on the electrode properties, i.e., the vacancy formation barrier E_b, as shown in Fig. 6a. Equation 8 is employed as the boundary condition for the $V_o^{\cdot\cdot}$ evolution (Eq. 4) at the anode/oxide interface where a positive external voltage is applied at the anode, as indicated in Fig. 6a. The grounded cathode is 50 nm Pt films for all cases and is assumed to be chemically inert, so that there is no oxygen exchange flux at the oxide/cathode interface.

For metal oxide-based RRAM, the CF is assumed to be in metallic phase consisting of high oxygen vacancy density. Therefore, the electroforming process can be considered a self-doping process, in which each oxygen vacancy acts as a donor that introduces two extra electrons. Thus, the local electrical conductivity of the oxide is strongly dependent on the oxygen vacancy density $N_{V_o^{\cdot\cdot}}$. The electrical conductivity is described by the Arrhenius equation[55–57], $\sigma = \sigma_0 e^{-\frac{E_{AC}}{k_B T}}$, where σ_0 is a pre-exponential factor and E_{AC} is the activation energy for conduction. Thus, both E_{AC} and σ_0 should depend on $N_{V_o^{\cdot\cdot}}$.

As shown in Fig. 6b, here we assume that σ_0 is linearly proportional to $N_{V_o^{\cdot\cdot}}$ with a slope of $K_1 = 2.38$ for HfO_{2-x}. This assumption is based on the previous experimental[38] and theoretical results[56]. In most metal oxide-based RRAM, the oxygen vacancies act as n-type donors[18,58,59], leading to a shift in the position of Fermi level. The region of lower oxygen vacancy density ($N_{V_o^{\cdot\cdot}} < 0.2 \times 10^{27}\ \mathrm{m^{-3}}$) shows semiconductor-like behavior, where E_{AC} is assumed to linearly increase from 0.0 to 0.05 eV with decreasing oxygen vacancies[56]. $E_{AC} = 0.05$ eV is consistent with the activation energy in reset state HfO_x[56]. For a high oxygen vacancy density ($N_{V_o^{\cdot\cdot}} > 0.2 \times 10^{27}\ \mathrm{m^{-3}}$), the activation energy E_{AC} is chosen to be 0.0 eV, which means that the Fermi level is pinned in the conduction band, corresponding to the metallic CF nature[18]. On the other hand, a linear relationship between k_{th} and $N_{V_o^{\cdot\cdot}}$ with a slope of $K_2 = 1.875$ for HfO_{2-x} materials is assumed due to the Joule heating effect, which is related to the ratio of electrical and thermal conductivity based on the Wiedemann–Franz Law[55,56], as shown in Fig. 6b. The minimum $k_{\mathrm{th}} = 0.5\ \mathrm{W\,m^{-1}K^{-1}}$ for $N_{V_o^{\cdot\cdot}} = 0$ is selected that corresponds to the thermal conductivity of the insulating HfO_2 material[60]. The maximum k_{th} value at high $N_{V_o^{\cdot\cdot}}$ corresponds to the metallic CF, which is equal to the thermal conductivity of metal hafnium ($23\ \mathrm{W\,m^{-1}K^{-1}}$)[61]. Based on the assumptions that σ and k_{th} are linearly proportional to the oxygen vacancy density $N_{V_o^{\cdot\cdot}}$, the electrical/thermal conductivity of different metal oxides can simply be represented by tuning the magnitudes of K_1 and K_2. This enables us to easily investigate the effects of the electrical and thermal conductivity of different metal oxides on the CF growth behavior.

The simulation involves the self-consistent solutions of the Nernst–Planck equation (Eq. 4) for $V_o^{\cdot\cdot}$ migration with a flux boundary condition defined by Eq. 8 at anode/oxide interface, the current continuity equation (Eq. 5) for electronic conduction, and the thermal transport equation (Eq. 7) for Joule heating. These equations are solved using finite element method based on the platform of COMSOL Multiphysics. The model reduces the 3D problem to 2D axisymmetric representation with a radial coordinate x and axial coordinate z, as illustrated in Fig. 6a. The total simulation size is $20 \times 80\ \mathrm{nm^2}$ and the mesh size is selected as 0.5 nm. The time step Δt in numerical simulation is chosen to be 0.01 s, allowing sufficient time for the oxygen vacancy transport to reach equilibrium at each time step, and ensures that the simulation results are independent of Δt. The metal oxide layer is connected with a top electrode ($x = 0$–20, $z = 10$–30 nm) where an external voltage is applied, and a bottom electrode ($x = 0$–20, $z = -50$–0 nm) which is grounded. The temperature at the surfaces of the two electrodes are fixed at 300 K.

DATA AVAILABILITY

The raw data in this paper are available from the corresponding authors (ye.cao@uta.edu) upon reasonable request.

Received: 4 November 2021; Accepted: 26 March 2022;
Published online: 21 April 2022

REFERENCES

1. Nam, Y. et al. Switchable Schottky diode characteristics induced by electroforming process in Mn-doped ZnO thin films. *Appl. Phys. Lett.* **102**, 162105 (2013).
2. Wang, Z. et al. Resistive switching materials for information processing. *Nat. Rev. Mater.* **5**, 173–195 (2020).
3. Zidan, M. A., Strachan, J. P. & Lu, W. D. The future of electronics based on memristive systems. *Nat. Electron.* **1**, 22–29 (2018).
4. Jo, S. H. et al. Nanoscale memristor device as synapse in neuromorphic systems. *Nano Lett.* **10**, 1297–1301 (2010).
5. Shen, Z. et al. Advances of RRAM devices: Resistive switching mechanisms, materials, and bionic synaptic application. *Nanomaterials* **10**, 1437 (2020).
6. Xia, Q. & Yang, J. J. Memristive crossbar arrays for brain-inspired computing. *Nat. Mater.* **18**, 309–323 (2019).
7. Yao, P. et al. Fully hardware-implemented memristor convolutional neural network. *Nature* **577**, 641–646 (2020).
8. Pedretti, G. & Ielmini, D. In-memory computing with resistive memory circuits: Status and outlook. *Electronics* **10**, 1063 (2021).
9. Ielmini, D. Resistive switching memories based on metal oxides: Mechanisms, reliability, and scaling. *Semicond. Sci. Technol.* **31**, 063002 (2016).
10. Hu, S. G. et al. Review of nanostructured resistive switching memristor and Its applications. *Nanosci. Nanotechnol. Lett.* **6**, 729–757 (2014).
11. Zahoor, F., Azni Zulkifli, T. Z. & Khanday, F. A. Resistive random access memory (RRAM): An overview of materials, switching mechanism, performance, multilevel cell (mlc) storage, modeling, and applications. *Nanoscale Res. Lett.* **15**, 90 (2020).
12. Lee, S. H., Zhu, X. & Lu, W. D. Nanoscale resistive switching devices for memory and computing applications. *Nano Res.* **13**, 1228–1243 (2020).
13. Kozicki, M. N., Park, M. & Mitkova, M. Nanoscale memory elements based on solid-state electrolytes. *IEEE Trans. Nanotechnol.* **4**, 331–338 (2005).

14. Guo, X., Schindler, C., Menzel, S. & Waser, R. Understanding the switching-off mechanism in Ag^{+} migration based resistively switching model systems. *Appl. Phys. Lett.* **91**, 133513 (2007).
15. Yalon, E. et al. Detection of the insulating gap and conductive filament growth direction in resistive memories. *Nanoscale* **7**, 15434–15441 (2015).
16. Ielmini, D. et al. Scaling analysis of submicrometer nickel-oxide-based resistive switching memory devices. *J. Appl. Phys.* **109**, 034506 (2011).
17. Jeong, D. S., Schroeder, H., Breuer, U. & Waser, R. Characteristic electroforming behavior in Pt/TiO_2/Pt resistive switching cells depending on atmosphere. *J. Appl. Phys.* **104**, 123716 (2008).
18. Ielmini, D., Nardi, F. & Cagli, C. Physical models of size-dependent nanofilament formation and rupture in NiO resistive switching memories. *Nanotechnology* **22**, 254022 (2011).
19. Bersuker, G. et al. Metal oxide resistive memory switching mechanism based on conductive filament properties. *J. Appl. Phys.* **110**, 124518 (2011).
20. Zhuang, H. L., Ganesh, P., Cooper, V. R., Xu, H. & Kent, P. R. C. Understanding the interactions between oxygen vacancies at $SrTiO_3$ (001) surfaces. *Phys. Rev. B* **90**, 064106 (2014).
21. Sharma, A. A. et al. Dynamics of electroforming in binary metal oxide-based resistive switching memory. *J. Appl. Phys.* **118**, 114903 (2015).
22. Zhou, X. et al. A high performance electroformed single-crystallite VO_2 threshold switch. *Nanoscale* **11**, 22070–22078 (2019).
23. Dirkmann, S., Kaiser, J., Wenger, C. & Mussenbrock, T. Filament growth and resistive switching in hafnium oxide memristive devices. *ACS Appl. Mater. Interfaces* **10**, 14857–14868 (2018).
24. Chen, Y. Y. et al. Endurance/retention trade-off on HfO_2/metal cap 1T1R bipolar RRAM. *IEEE Trans. Electron Devices* **60**, 1114–1121 (2013).
25. Sun, P. et al. Physical model for electroforming process in valence change resistive random access memory. *J. Comput. Electron.* **14**, 146–150 (2014).
26. Chakraverty, B. K. Metal–insulator transition; nucleation of a conducting phase in amorphous semiconductors. *J. Non-Cryst. Solids* **3**, 317–326 (1970).
27. Nandi, S. K., Liu, X., Venkatachalam, D. K. & Elliman, R. G. Effect of electrode roughness on electroforming in HfO_2 and defect-induced moderation of electric-field enhancement. *Phys. Rev. Appl.* **4**, 064010 (2015).
28. Xu, X., Rajendran, B. & Anantram, M. P. Kinetic Monte Carlo simulation of interface-controlled hafnia-based resistive memory. *IEEE Trans. Electron Devices* **67**, 118–124 (2020).
29. Noman, M. et al. Mechanism of localized electrical conduction at the onset of electroforming in TiO_2 based resistive switching devices. *Appl. Phys. Lett.* **104**, 113510 (2014).
30. Ielmini, D., Cagli, C. & Nardi, F. Resistance transition in metal oxides induced by electronic threshold switching. *Appl. Phys. Lett.* **94**, 063511 (2009).
31. Kamiya, K. et al. ON-OFF switching mechanism of resistive-random-access-memories based on the formation and disruption of oxygen vacancy conducting channels. *Appl. Phys. Lett.* **100**, 073502 (2012).
32. Clima, S. et al. First-principles simulation of oxygen diffusion in HfO_x: Role in the resistive switching mechanism. *Appl. Phys. Lett.* **100**, 133102 (2012).
33. Yang, J. J. et al. The mechanism of electroforming of metal oxide memristive switches. *Nanotechnology* **20**, 215201 (2009).
34. Nandi, S. K. et al. Electric field- and current-induced electroforming modes in NbO_x. *ACS Appl. Mater. Interfaces* **12**, 8422–8428 (2020).
35. Zhang, K. et al. High-throughput phase-field simulations and machine learning of resistive switching in resistive random-access memory. *NPJ Comput. Mater.* **6**, 198 (2020).
36. Chen, Y.-C. et al. Dynamic conductance characteristics in HfO_x-based resistive random access memory. *RSC Adv.* **7**, 12984–12989 (2017).
37. Chudnovskii, F. A., Odynets, L. L., Pergament, A. L. & Stefanovich, G. B. Electroforming and switching in oxides of transition metals: the role of metal-insulator transition in the switching mechanism. *J. Solid State Chem.* **122**, 95–99 (1996).
38. Nardi, F., Larentis, S., Balatti, S., Gilmer, D. C. & Ielmini, D. Resistive switching by voltage-driven ion migration in bipolar RRAM-part I: Experimental study. *IEEE Trans. Electron Devices* **59**, 2461–2467 (2012).
39. Sharath, S. U. et al. Impact of oxygen stoichiometry on electroforming and multiple switching modes in TiN/TaO_x/Pt based ReRAM. *Appl. Phys. Lett.* **109**, 173503 (2016).
40. Chand, U. et al. Suppression of endurance degradation by utilizing oxygen plasma treatment in HfO_2 resistive switching memory. *Appl. Phys. Lett.* **106**, 153502 (2015).
41. Wu, Q. et al. Improvement of durability and switching speed by incorporating nanocrystals in the HfO_x based resistive random access memory devices. *Appl. Phys. Lett.* **113**, 023105 (2018).
42. Lee, H. Y. et al. Low power and high speed bipolar swithing with a thin reactive Ti buffer layer in robust HfO_2 based RRAM. In *2008 IEEE International Electron Devices Meeting* 1–4 (IEEE, 2008).
43. Huang, J. J., Kuo, C. W., Chang, W. C. & Hou, T. H. Transition of stable rectification to resistive-switching in Ti/TiO_2/Pt oxide diode. *Appl. Phys. Lett.* **96**, 262901 (2010).
44. Wei, Z. et al. Highly reliable TaO_x ReRAM and direct evidence of redox reaction mechanism. In *2008 IEEE International Electron Devices Meeting* 1–4 (IEEE, 2008).
45. Yang, J. J. et al. High switching endurance in TaO_x memristive devices. *Appl. Phys. Lett.* **97**, 232102 (2010).
46. Yoon, J. H. et al. Highly uniform, electroforming-free, and self-rectifying resistive memory in the Pt/Ta_2O_5/HfO_{2-x}/TiN Structure. *Adv. Funct. Mater.* **24**, 5086–5095 (2014).
47. Ganesh, P. et al. Doping a bad metal: Origin of suppression of the metal-insulator transition in nonstoichiometric VO_2. *Phys. Rev. B* **101**, 155129 (2020).
48. Lee, S. et al. Anomalously low electronic thermal conductivity in metallic vanadium dioxide. *Science* **355**, 371–374 (2017).
49. Abbaspour, E., Menzel, S. & Jungemann, C. The role of the interface reactions in the electroforming of redox-based resistive switching devices using KMC simulations. In *Int. Conf. Simul. Semicond. Process. Devices SISPAD* 293–296 (IEEE, 2015).
50. Ielmini, D., Nardi, F. & Cagli, C. Universal reset characteristics of unipolar and bipolar metal-oxide RRAM. *IEEE Trans. Electron Devices* **58**, 3246–3253 (2011).
51. Abbaspour, E., Menzel, S. & Jungemann, C. KMC simulation of the electroforming, set and reset processes in redox-based resistive switching devices. In *Int. Conf. Simul. Semicond. Process. Devices SISPAD* 141–144 (2016).
52. Aspera, S. M. et al. Realization of the switching mechanism in resistance random access memory™ devices: Structural and electronic properties affecting electron conductivity in a hafnium oxide-electrode system through first-principles calculations. *J. Electron. Mater.* **42**, 143–150 (2012).
53. Padovani, A. et al. Understanding the role of the Ti metal electrode on the forming of HfO_2-based RRAMs. In *2012 4th IEEE International Memory Workshop* 1–4 (IEEE, 2012).
54. Bersuker, G. et al. Grain boundary-driven leakage path formation in HfO_2 dielectrics. *Solid State Electron.* **65–66**, 146–150 (2011).
55. Kim, S. et al. Physical electro-thermal model of resistive switching in bi-layered resistance-change memory. *Sci. Rep.* **3**, 1680 (2013).
56. Larentis, S., Nardi, F., Balatti, S., Gilmer, D. C. & Ielmini, D. Resistive switching by voltage-driven ion migration in bipolar RRAM-part II: Modeling. *IEEE Trans. Electron Devices* **59**, 2468–2475 (2012).
57. Kim, S., Choi, S. & Lu, W. Comprehensive physical model of dynamic resistive switching in an oxide memristor. *ACS Nano* **8**, 2369–2376 (2014).
58. Zhang, C., Liu, G., Geng, X., Wu, K. & Debliquy, M. Metal oxide semiconductors with highly concentrated oxygen vacancies for gas sensing materials: A review. *Sens. Actuator A Phys.* **309**, 112026 (2020).
59. Zheng, X. D. The influence of ion implantation-induced oxygen vacancy on electrical conductivity of WO_3 thin films. *Vacuum* **165**, 46–50 (2019).
60. Panzer, M. A. et al. Thermal properties of ultrathin hafnium oxide gate dielectric films. *IEEE Electron Device Lett.* **30**, 1269–1271 (2009).
61. Milošević, N. D. & Maglić, K. D. Thermophysical properties of solid phase hafnium at high temperatures. *Int. J. Thermophys.* **27**, 530–553 (2006).

ACKNOWLEDGEMENTS

K.Z. and Y.C. acknowledge the support from the National Science Foundation (NSF) under the award number NSF 2132105, and the Texas Advanced Computing Center (TACC) at The University of Texas at Austin for providing HPC resources that have contributed to the research results reported within this paper (http://www.tacc.utexas.edu). Y.C. also acknowledges the startup funding from the University of Texas at Arlington. P.G. (physical model, analysis and interpretation) was supported by the Center for Nanophase Materials Sciences, which is a DOE Office of Science User Facility.

AUTHOR CONTRIBUTIONS

Y.C conceived and designed the study. K.Z. developed the models and performed all simulations under the guidance of Y.C. All authors contributed to interpreting the results and writing of the paper.

COMPETING INTERESTS

The authors declare no competing interests.

ADDITIONAL INFORMATION

Supplementary information The online version contains supplementary material available at https://doi.org/10.1038/s41524-022-00770-2.

Correspondence and requests for materials should be addressed to Ye Cao.

Reprints and permission information is available at http://www.nature.com/reprints

Publisher's note Springer Nature remains neutral with regard to jurisdictional claims in published maps and institutional affiliations.

Open Access This article is licensed under a Creative Commons Attribution 4.0 International License, which permits use, sharing, adaptation, distribution and reproduction in any medium or format, as long as you give appropriate credit to the original author(s) and the source, provide a link to the Creative Commons license, and indicate if changes were made. The images or other third party material in this article are included in the article's Creative Commons license, unless indicated otherwise in a credit line to the material. If material is not included in the article's Creative Commons license and your intended use is not permitted by statutory regulation or exceeds the permitted use, you will need to obtain permission directly from the copyright holder. To view a copy of this license, visit http://creativecommons.org/licenses/by/4.0/.

© The Author(s) 2022